International Journal of Hydrogen Energy 221 (2026) 154185

Contents lists available at ScienceDirect

International Journal of Hydrogen Energy

journal homepage: www.elsevier.com/locate/he

Hydrogen-based direct reduction of steel by-product mill scale

Bénédicte Kuypers [a], Nicole C. Stevens [b,c], Conrad J.M. Hessels [b,c], Pascal J. Jacques [a], Giulia Finotello [b,c], Laurine Choisez [a,*]

[a] UCLouvain, Institute of Mechanics, Materials and Civil Engineering, IMAP, Place Sainte 2, B-1348, Louvain-la-Neuve, Belgium
[b] Power and Flow Group, Department of Mechanical Engineering, Eindhoven Institute for Renewable Energy Systems, PO Box 513, 5600, MB Eindhoven, Netherlands
[c] Eindhoven Institute for Renewable Energy Systems (EIRES), PO Box 513, 5600, MB, Eindhoven, Netherlands

ARTICLE INFO

Keywords:
Low carbon steel production
Hydrogen-based direct reduction
Pre-oxidation
Mill scale

ABSTRACT

Hydrogen-based direct reduction (HyDR) of mill scale is a promising process for transitioning the steel industry towards more sustainable production. Previous studies focused on high temperature reduction of mill scale in shaft furnace, but sintering issues are encountered. To mitigate this problem, the reduction of mill scale particles was investigated at lower temperatures (400°C-700 °C). Reduction experiments were conducted in a thermogravimetric analyzer (TGA) using pure hydrogen, both with and without pre-oxidation stage conducted between 700 °C and 900 °C and coupled with microstructure characterization. The highest reduction rate is obtained at 500 °C after pre-oxidation at 800 °C, governed by mixed phase boundary and 2D nucleation and growth mechanisms. Without pre-oxidation, unstable wüstite decomposes into Fe and Fe_3O_4 as analyzed under both neutral and reducing atmosphere following a 1D nucleation and growth mechanism, while magnetite reduction to iron is governed by a phase boundary-limited mechanism.

1. Introduction

The urgent transition towards a more sustainable society must include a reduction in greenhouse gases produced by the steel production sector, estimated at around 5% of CO_2 emissions in Europe and almost 7% worldwide [1]. The decarbonization of steel production relies on the shift in the primary production methods (reduction agents) and on additional recycling of steel. In 2016, 70% of the world's steel was produced by blast furnaces or basic oxygen furnaces [2]. This production method is energy-intensive (about 18 GJ/t of crude steel due to high-temperature operation, coking coal, hot air injection, etc. [3]) and also highly polluting due to the use of carbon-based reducing agents (coke and coal). A promising alternative is the use of hydrogen gas as a reducing agent to produce metal with a lower environmental impact. Indeed, 0.1 ton of CO_2 could be emitted per ton of steel if sustainably produced hydrogen were used, compared to 1.9 tons of CO_2 per ton of steel for conventional blast furnace production [4]. These emissions can be further reduced by recycling iron-rich sources, such as mill scale, a low-cost iron-based industrial by-product (containing about 70 wt % of iron [5]). It corresponds to approximately 2% of the steel related waste mass [5], thus about 18.4 millions of tons produced worldwide in 2024 [6]. This huge amount is already mostly recycled in integrated steel plants, with up to 85% of the produced mill scale consumed via sintering of mill scale mixed with iron [5], directly re-injected in the steel-making process. The remaining 15% is not suitable for recycling due to its properties or contamination [5]. Improving the level of direct recycling of mill scale is sometimes not possible (logistical issues, quality/adequacy of the mill scale …) and landfilling is the current chosen solution. Developing an alternative path for the upcycling of this by-product is thus of interest.

In this work, the recycling of mill scale fines is considered for a new high-density energy storage technology called iron fuel [7]. Sustainable energy can be stored by direct chemical reduction of the iron oxide powder, and released through its high-temperature oxidation in air or water [8]. The presence of chemical additions naturally present in the mill scale was found to be very promising for the iron fuel cycle [9,10]. For this application, the aimed products are therefore a fine reduced mill-scale powder in the range of 30 μm – 100 μm.

Reduction of mill scale pellets of size ranging from 2 to 25 mm as well as powder particles with sizes smaller than 200 μm, with mainly Ca, Si, Mn, Al, Cu and Cr oxides impurities, into metallic iron has previously been proved possible using carbon-based reducing agents (coke, coal, CO/CO_2 mixture, anthracite) at high temperatures (700 °C – 1200 °C) [11–19]. Less studies were conducted using hydrogen as the reducing

* Corresponding author.
E-mail address: laurine.choisez@uclouvain.be (L. Choisez).

https://doi.org/10.1016/j.ijhydene.2026.154185
Received 21 August 2025; Received in revised form 18 January 2026; Accepted 21 February 2026
Available online 28 February 2026

agent, and they were all carried out at high temperatures (600 °C – 1300 °C) in vertical or tubular furnaces [20–26]. This temperature range is typically aimed at the industrial scale, where hydrogen-based direct reduction of iron ores is mainly conducted in shaft furnaces with operating temperatures close to 800°C – 1000 °C [27,28]. In that case, the ores fines need to be first pelletized. To avoid pelletization and obtain powders as the reduction products, fluidized bed reactors are an interesting alternative pathway. However, the operating reduction temperatures in fluidized bed reactors are limited due to powder agglomeration and defluidization at high temperatures. The operating temperatures for direct reduction in fluidized bed reactors must be under 500 °C – 700 °C for particle sizes of 50 μm – 200 μm [29].

Guan et al. [30] studied the reduction of mill scale crust (2 mm thick) at 370 °C – 550 °C using Ar–H_2 (20-80 vol %) in a thermogravimetric analyzer. Complete reduction of the oxidized crust was achieved, with the reduction time decreasing with an increasing temperature [30]. Nevertheless, reduction of mill scale fines (<150 μm) under pure hydrogen in this temperature range remains unexplored.

Furthermore, pre-oxidation of magnetite-based iron ore consistently demonstrated improved reduction rates [31–34], although it has never been applied to mill scale particles. The reduction of magnetite is promoted by the increased number of defects from the oxidation step, favoring diffusion and formation of pores during reduction, according to Edström [35]. Wang et al. [36] also observed a positive influence of pre-oxidation for the reduction of ironsand, mainly composed of wüstite with oxides inclusions (TiO_2, SiO_2, MgO, Al_2O_3, CaO).

In this work, hydrogen-based direct reduction of mill scale fines (45 μm – 106 μm) was investigated in the temperature range of 400 °C – 700 °C, with and without applying a pre-oxidation step in the temperature range of 700 °C – 900 °C. A combination of thermogravimetric analyses, thermal treatments and microstructural characterizations (SEM, XRD, BET surface area, gas pycnometry) was conducted to identify the fundamental mechanisms governing the reduction kinetics. The importance of wüstite decomposition on its reduction under 570 °C was highlighted.

2. Material and methods

2.1. Material and characterization techniques

Representative of industrial mill scale collected after descaling steel slabs, prior to hot rolling, was considered in this work. The mean chemical composition given in Table 1 was measured by inductively coupled plasma (ICP-OES) analysis and total carbon content analysis (TCC), and averaged over ten samplings. After drying for 2 h at 120 °C in air to remove moisture, the broken crust was further ground by ring milling and sieved to collect particles with sizes between 45 and 106 μm. Fig. 1 presents the size distribution (Fig. 1b) and sphericity (Fig. 1c) of the obtained mill scale powder, measured by laser diffraction and image analysis using the wet mode with 2 vol % of tetrasodium pyrophosphate in water as dispersant over three samplings. The majority (80%) of the particles ranges between 10 and 130 μm, with a mean diameter and standard deviation of the volume-based distribution of 60.8 μm and 48.8 μm, respectively. Smaller particles of hundreds of nanometers in diameter could not be fully separated from the main particles by the sieving process, likely due to van der Waals forces, as illustrated in Fig. 1b and d. The Dv10, Dv50, and Dv90 (indicating the upper size limit containing 10%, 50% and 90% of the powder volume) were of 3.2 μm, 54.0 μm and 112.9 μm, respectively. On the other hand, the powder presents a relatively low sphericity, reflecting the irregular shape of the particles, given by the sphericity distribution in Fig. 1c and as illustrated by the scanning electron microscopy (SEM) observations of Fig. 1d and e. Additionally to the irregular shape, deposits were also observed on the surface, as shown in Fig. 1f at higher magnification. Energy-dispersive X-ray (SEM-EDX) analyses (carried out at 15 kV) indicate local variations of the chemical composition with higher levels of elements other than Fe detected among these deposits (Fig. S1 in Supplementary Material), based on more than 10 measurements points for each characterized microstructure. These additional elements are more present on the surface deposits than within mill scale particles (Supplementary Fig. S2). From EDX analyses on cross sections, manganese was detected as the main foreign element dissolved in solid solution in the iron oxides (average 0.76 wt % with a 0.13 wt % standard deviation). Other additional elements are also present as oxide precipitates (*e.g.* chromium oxides as illustrated in Fig. S1 in Supplementary Material).

The average volume fractions of each phase were quantified by X-ray diffraction and Rietveld refinement using *TOPAS* V5.0 after manual powder grinding, using a cobalt source at 30 kV and 30 mA. The only fitting parameters used for Rietveld refinement were the lattice parameters and the crystallite size of each phase. No additional corrections were applied to avoid overfitting. The average mass fractions of each phase was estimated from the measured average volume fractions using 5.26 g/cm^3, 5.19 g/cm^3, 5.95 g/cm^3 and 7.87 g/cm^3 as the theoretical densities of Fe_2O_3, Fe_3O_4, $Fe_{1-x}O$ and Fe, respectively [37]. The initial mass fraction of each phase in the initial mill scale is given in Table 2 for three different samplings.

The same characterization techniques (SEM, EDX, ICP and TCC, XRD) were used to characterize the pre-oxidized and reduced mill scale powders. Moreover, the surface area evolution was measured by the Brunauer-Emmett-Teller (BET) method, with Krypton gas (purity 99.999%), using the BET method with a p/p_0 range from 0.05 to 0.30. The data were corrected to ensure a continuous increase in $V(1-p/p_0)$, with V the molar volume of adsorbed gas, p the equilibrium pressure and p_0 the pressure at saturation of the adsorbed gas. The closed, non-percolating porosity was estimated using a gas pycnometer with nitrogen gas in combination with the theoretical solid phase densities.

2.2. Thermogravimetry analysis (TGA)

The reaction kinetics are measured in a thermogravimetric analyzer (TGA), developed by Coenen et al. [38]. The reactor (a quartz tube with a 19 mm diameter and 1.5 mm wall thickness) is kept at the desired temperature by resistive heating inside an insulating assembly. The sample, 100 mg of powder, is placed in an aluminum-oxide crucible (5 mm inner diameter, 10 mm height and 1 mm wall thickness), suspended to a micro-balance with a sensitivity of 0.1 μg by a titanium wire and placed in controlled gas flows.

To analyze the kinetics and reduction mechanisms of iron oxides, three types of experiments are carried out: (1) full or partial hydrogen-based reduction (HyDR) of as-received mill scale, (2) full pre-oxidation of initial mill scale, (3) full pre-oxidation followed by full or partial HyDR. Reduction is carried out at three different temperatures below 570 °C (400 °C, 450 °C and 500 °C) to calculate the apparent activation energy of reduction when wüstite is not stabilized. The impact of wüstite stabilization above 570 °C is additionally studied at 700 °C, sufficiently far away from the transition zone. Three pre-oxidation temperatures

Table 1
Mean chemical composition of initial mill scale particles, measured by ICP and total carbon content analysis. The average and standard deviation are given over 10 samplings.

[wt %]	Fe	Mn	Al	Si	Cr	Cu	Ni	Mg	C^{tot}	O
Avg	73.46	0.37	0.05	0.04	0.02	0.02	0.02	<0.01	0.24	Rest
Std	0.83	0.03	0.01	0.01	0.01	<0.01	0.02	<0.01	0.18	/

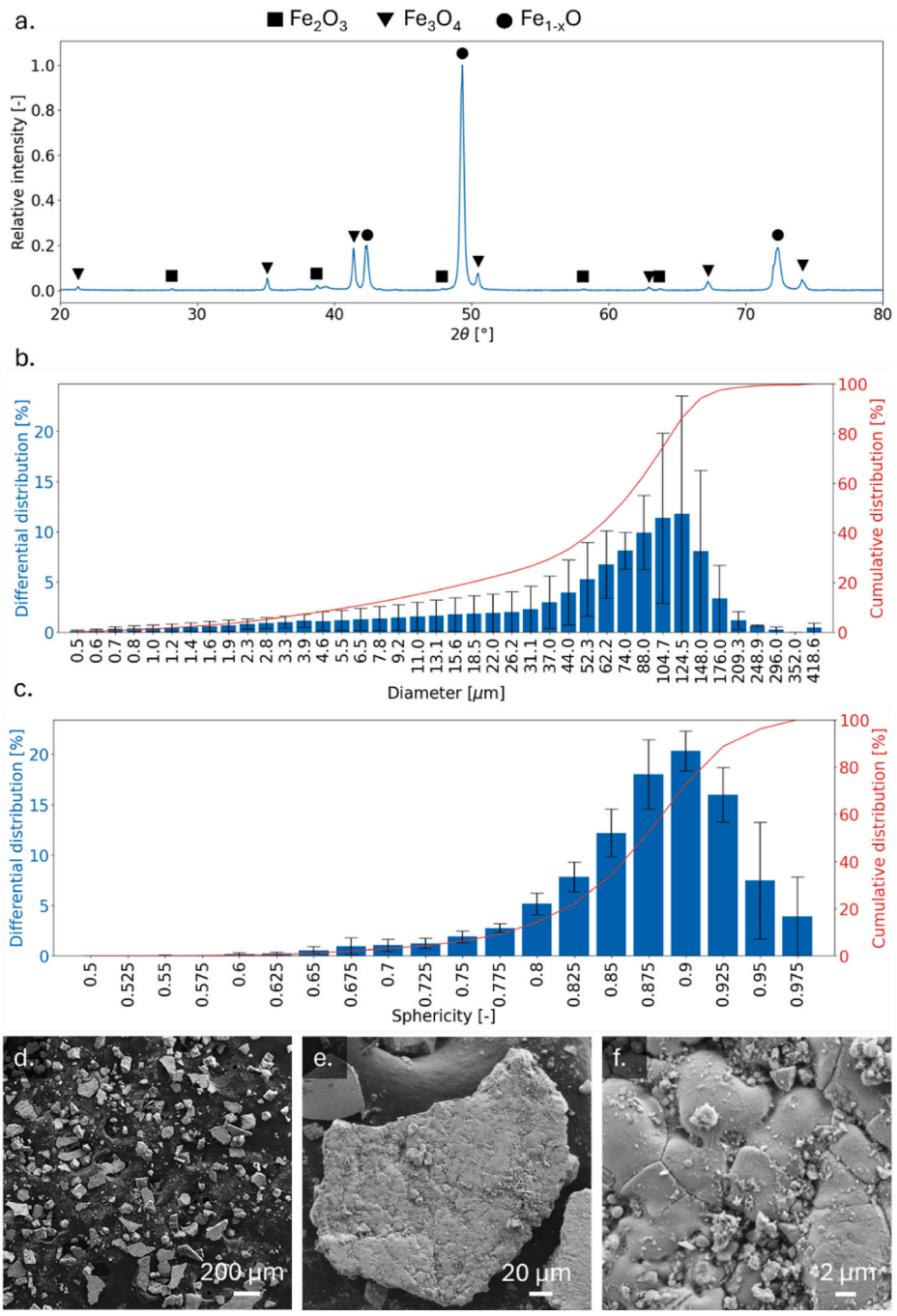

Fig. 1. Characterization of the initial mill scale particles. (a) X-ray diffraction spectrum. (b) Particles size and (c) sphericity distributions (volume-based) of the sieved particles (45-106 μm) measured and averaged by dynamic image analysis over 3 samplings. (d) (e) (f) SEM micrographs of the initial particles at different magnifications (SE2 signal).

Table 2
Phase distribution in as-received mill scale, measured by X-ray diffraction and Rietveld refinement, given as the average and standard deviation over three samplings.

[wt %]	Fe	$Fe_{1-x}O$	Fe_3O_4	Fe_2O_3
Average	0	81.5	16.0	2.5
Standard deviation	0	2.1	2.0	0.6

(700 °C, 800 °C, 900 °C) are chosen based on their positive impact reported in the literature [31,32,36,39,40].

In the case of HyDR, nitrogen gas (500 milli-NLPM) is used during heating (20 °C/min rate). Once the reactor is stabilized at the desired temperature (400 °C, 450 °C, 500 °C or 700 °C), hydrogen gas (99.999%) at 480 milli-NLPM is fed in for a maximum of 3 h if a full reduction is desired. The reaction is stopped sooner if the change in mass in the last 30 min is less than 0.5 mg in case of the full reduction tests, or at the aimed reaction duration for the partial reduction tests. During cooling, the reactor is switched back to a flow of nitrogen (500 milli-NLPM) and is cooled down as fast as possible (cooling rate varying between 30 °C/min and 50 °C/min). In the case of pre-oxidation, the same heating and cooling procedures are applied, but a flow of air (79% nitrogen and 21% oxygen, at 480 milli-NLPM) is provided during the oxidation step. Pre-oxidation was carried out for 3 h at 800 °C and

900 °C, or for 4 h at 700 °C as full oxidation is targeted. Longer pre-oxidation time was chosen at 700 °C to partially compensate for the slower oxidation kinetics. In the case of HyDR following pre-oxidation, the sample was cooled down to the aimed reduction temperature under nitrogen in between the oxidation and reduction steps. The local variations in temperature and gas composition were minimized by using a relatively small sample amount (~100 mg) and large hydrogen flow rate (480 milli-NLPM). During the reduction reactions, the thermodynamic stability domain, given by the local temperature and the ratio between the gaseous reductant (hydrogen) and products (hydrogen + water vapor), was always kept in the reduced iron domain. The maximum water vapor production rate was reached during the reduction of pre-oxidized mill scale at 700 °C, and corresponded to a ratio between the gaseous reductant and products of 0.87, far above the thermodynamic limit of ~0.65. During pre-oxidation, the maximum oxygen consumption rate corresponded to a maximum decrease in oxygen concentration from 21% to 19.5%. The influence of local temperature and gas composition variations was therefore considered as negligible in our analysis.

The conversion degree is computed based on the measured mass evolution:

$$X(t) = \frac{m_{Fe_2O_3} - m(t)}{m_{Fe_2O_3} - m_{Fe,f}} \quad (1)$$

where $m_{Fe_2O_3}$ is the mass if completely oxidized to hematite, $m(t)$ is the measured mass at time t and $m_{Fe,f}$ is the final mass if completely reduced to iron (theoretically estimated from XRD measurements). The initial and final masses measured by TGA ($m(t)$) were corrected based on initial and final weighting, as well as on the final conversion degree measured by XRD. The conversion rate dX/dt can be derived from Equation (1), and was smoothed using a Savitzky-Golay filter (polyorder 2) with a window of 100 and 10 in the case without and with pre-oxidation, respectively (a Savitzky-Golay filter with a window of 40 and poly-order 3 has been applied a second time at the center of the curve at 450 °C without pre-oxidation to smooth it further). A fixed window is used to have a controllable and locally reproducible model over the entire curve. A maximum latency of 1.5 min is expected due to the window size and acquisition time interval (negligible regarding the long duration for full conversion i.e. 25-125 min).

Large variations of mass were recorded for reduction conducted at 450 °C and interpolation correction was applied to have an analyzable trend (Fig. S4 in Supplementary Material). Interrupted reduction tests were carried out for different reaction durations, giving a better understanding of the evolution of the phases and their mechanisms. For the case with pre-oxidation, reduction has been stopped after 30s, 100s and 390s, corresponding to 8%, 20% and 65% conversion, respectively. On the other hand, reduction of the as-received mill scale was interrupted after 42s and 980s, corresponding to 34% and 95% conversion (initial conversion of mill scale without pre-oxidation is around 25%).

2.3. Heat treatments

The decomposition of wüstite under 570 °C was decorrelated from its reduction by conducting several heat treatments in neutral atmosphere, using sealed quartz tubes filled with neutral nitrogen and ~2 g of mill scale powder. They were heated in a resistive furnace at a heating rate of ~15 °C/min up to 500 °C, maintained isothermally for 0 s, 42 s, 1000 s, 1 h, 2 h and 3 h, and then water quenched. The microstructures of the heat-treated powders were investigated using SEM and XRD, following the same procedure as described in Section 2.2. The lattice parameters of each phase were estimated during the integration of peaks using *Topas Software* (Section 2.1). The ratio of iron and oxygen associated with the wüstite phases was calculated based on the work of Berthon et al. [41].

3. Results

3.1. Pre-oxidation stage

Fig. 2 presents the oxidation kinetics (Fig. 2a) of mill scale at 700 °C, 800 °C or 900 °C and the reduction kinetics (Fig. 2b) at 500 °C for pre-oxidized mill scale at the three different pre-oxidation temperatures. 500 °C was chosen as the screening temperature here as it gave the most promising reduction kinetics in the non-oxidized case (see Section 3.2.1, Fig. 4). Complete oxidation to hematite is only reached with a pre-oxidation temperature of 900 °C. Slower oxidation kinetics are obtained at 800 °C and 700 °C, leading to a mix of 83-17 wt % and 50-50 wt % hematite-magnetite, respectively. The powder pre-oxidized at 800 °C presents the highest reduction rate at 500 °C and is chosen for the following reduction analyses.

Typical surface morphologies (Fig. 3a, b and c) and cross-section micrographs (Fig. 3d–i) of oxidized particles at 700 °C, 800 °C and 900 °C are shown in Fig. 3. The porous structure at the surface is the most commonly observed feature, although other morphologies (denser, vein-like, needles) are also detected on a few particles, as shown in Supplementary Fig. S3. A rougher, more porous, outer surface is observed at lower pre-oxidation temperature, consisting of more angular, geometric features. Smoother features are formed at higher temperatures. A denser outer layer is observed at 900 °C, where closed pores are highlighted by white arrows in Fig. 3c. Inside the particles, an inhomogeneous distribution of porosities is observed, with an accumulation of very small pores close to the initial particle contour. This is best shown on Fig. 3g and h with the initial surface highlighted by the dotted lines. Delamination is also visible between the outer-grown oxide scale and the initial particle contour at every temperature, as highlighted by the white arrow in Fig. 3d.

3.2. Hydrogen-based direct reduction

3.2.1. Influence of reduction temperature and pre-oxidation state

Fig. 4 presents the overall reduction kinetics of the mill scale particles measured by the thermogravimetric analyzer, with the mill scale particle reduced as received in Fig. 4 (a), (b) and after a pre-oxidation at 800 °C in Fig. 4(c) and (d). Increasing the reduction temperature from 400 °C to 450 °C shortens the time to reach 90% conversion by a factor 3. Raising the temperature to 500 °C further reduces this time by a factor of 2. The conversion rate always presents a sharp increase in the beginning of the reaction, followed by a stabilization and slow decrease with further conversion. The initial conversion rate is systematically increased with the reduction temperature, but significantly slows down around a conversion degree of 0.41 at 700 °C. In Fig. 4a, this results in a stabilization of the conversion degree around 92% and complete conversion is therefore not achieved even after 3 h of reduction. On the other hand, at every temperature, applying an oxidation step prior to the reduction results in a faster reaction rate (Fig. 4b). At 700 °C, pre-oxidation increases both the initial reduction rate (from 0.06 to 0.28 min^{-1}) and the stabilization of the conversion degree (from 92 to 95% conversion after 3 h).

Fig. 5 illustrates the surface morphologies, before and after reduction at 400 °C – 700 °C, with and without pre-oxidation. For the *as-received* particles (Fig. 5a–e), the initial deposits at the surface of the particles (see Supplementary Figs. S1 and S2) are replaced by spheres of a few nanometers in diameter, increasing in size up to tens or hundreds of nm at 700 °C. On the other hand, when a pre-oxidation step is carried out, a rougher and more porous surface is observed (Fig. 5f–j). For a reduction at 700 °C (Fig. 5j), a coarser network can be seen. The pore size at the surface is increasing with temperature, going from about 0.1 μm at 400°C – 500 °C to 1 μm at 700 °C.

Cross-section micrographs of reduced mill scale particles at 500 °C and 700 °C with and without pre-oxidation are given in Fig. 6. Very different microstructure and morphology are observed when the

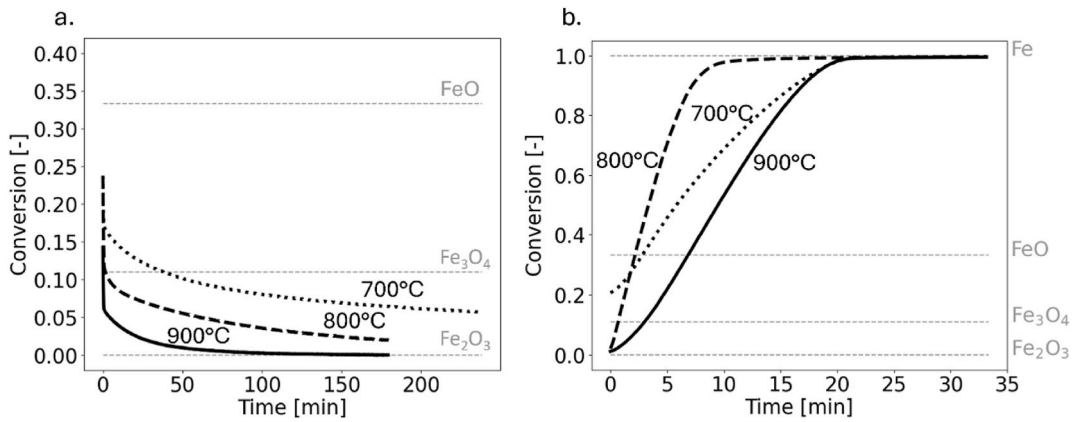

Fig. 2. Kinetics evolution for (a) pre-oxidation at 700 °C, 800 °C or 900 °C and (b) reduction at 500 °C after a pre-oxidation step at 700 °C, 800 °C or 900 °C.

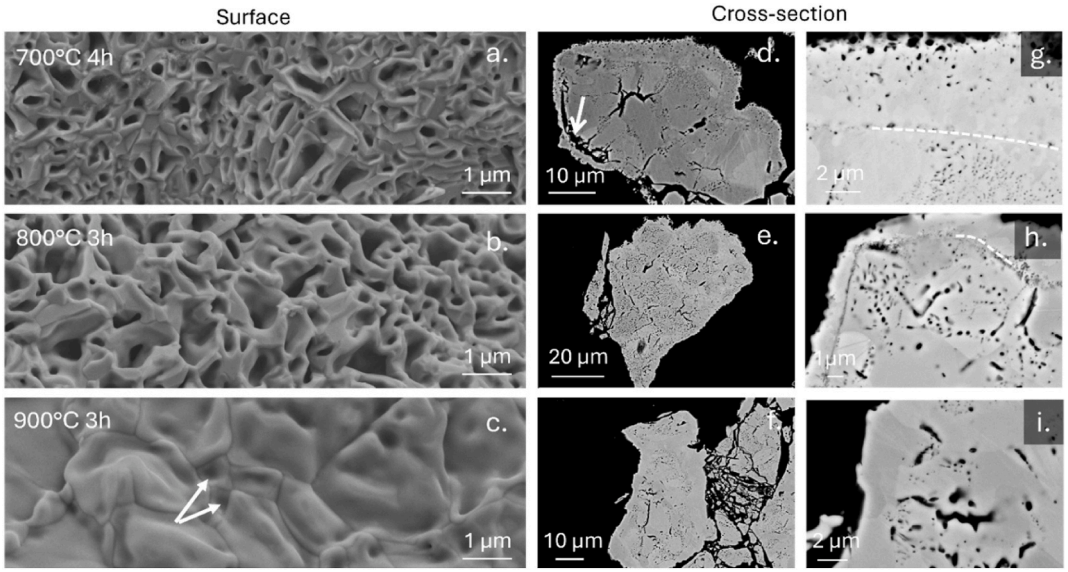

Fig. 3. Scanning Electron Micrographs of (a-c) the surface morphology (secondary electron signal) and (d-i) cross-section (backscattered signal) of particles pre-oxidized at (a), (d), (g) 700 °C for 4 h, (b), (e), (h) 800 °C for 3 h and (c), (f), (i) 900 °C for 3 h. The arrows in subfigures (c) and (d) indicate closed pores and delamination, respectively. The dotted lines in subfigures (g) and (h) delimit the initial contour of the particle.

reduction temperature is increased. This is due to the change in the reduction mechanisms with the appearance of wüstite, as further discussed in Sections 4.3.1 and 4.3.2. No significant differences in porosities are noted at 500 °C (Fig. 6b and e). At 700 °C (Fig. 6c and f), a significant proportion of wüstite (grey phase) remains surrounded by metallic iron (white phase), both with and without pre-oxidation.

Fig. 7a presents the influence of pre-oxidation and reduction on the volume of closed non-percolating porosity. Pre-oxidation at 700 °C does not induce significant porosity change, but the closed porosity content increases from 5.71 vol % to ~11.7 vol % after pre-oxidation at 800 °C and 900 °C. Reduction at 500 °C systematically increases the volume of closed porosity. Applying a pre-oxidation step leads to a higher initial content of non-percolating porosity. Fig. 7b presents the evolution of the closed porosity volume for different reduction temperatures. The application of a pre-oxidation step systematically decreases the closed porosity content at the end of the reduction process, except at 500 °C where the closed porosity stayed similar with and without applying a pre-oxidation step. Furthermore, the evolution of the surface area of the particles with the influence of pre-oxidation is given in Fig. 7c and with the influence of reduction temperatures in Fig. 7d. The surface area after oxidation at 900 °C lies below the detection limit and no data could have been extracted. From Fig. 7c, no effect on the initial surface area is observed due to the oxidation step, but reduction significantly increases the final surface area. On the other hand, a higher surface area is obtained for lower reduction temperatures (Fig. 7d). Applying a pre-oxidation step reduces the final surface area.

3.2.2. Microstructure evolution during hydrogen-based direct reduction at 500 °C

Partial reduction experiments were conducted to characterize the microstructure evolution during reduction at 500 °C. The proportions of phases detected by XRD in the as-received/pre-oxidized and partially reduced samples at 500 °C are given in Table 3.

Fig. 8 presents cross section SEM micrographs, coupled with EBSD analysis, of the three samples partially reduced (8%, 20% and 65%) following a pre-oxidation stage. Nucleation of metallic iron at the border of the particle and grain boundaries is already seen after 8% of conversion, as highlighted by the yellow arrows in Fig. 8c. Following reduction up to 20% (Fig. 8d–f), a growth of the iron phase is observed around the metallic iron nuclei previously formed at the surface or near cracks. For a reduction up to 65%, the reduced phase is surrounding the remaining oxidized grains, as shown in Fig. 8g–i.

On Fig. 9, cross section micrographs of the partially reduced samples without pre-oxidation are presented, coupled with EBSD analysis. As-

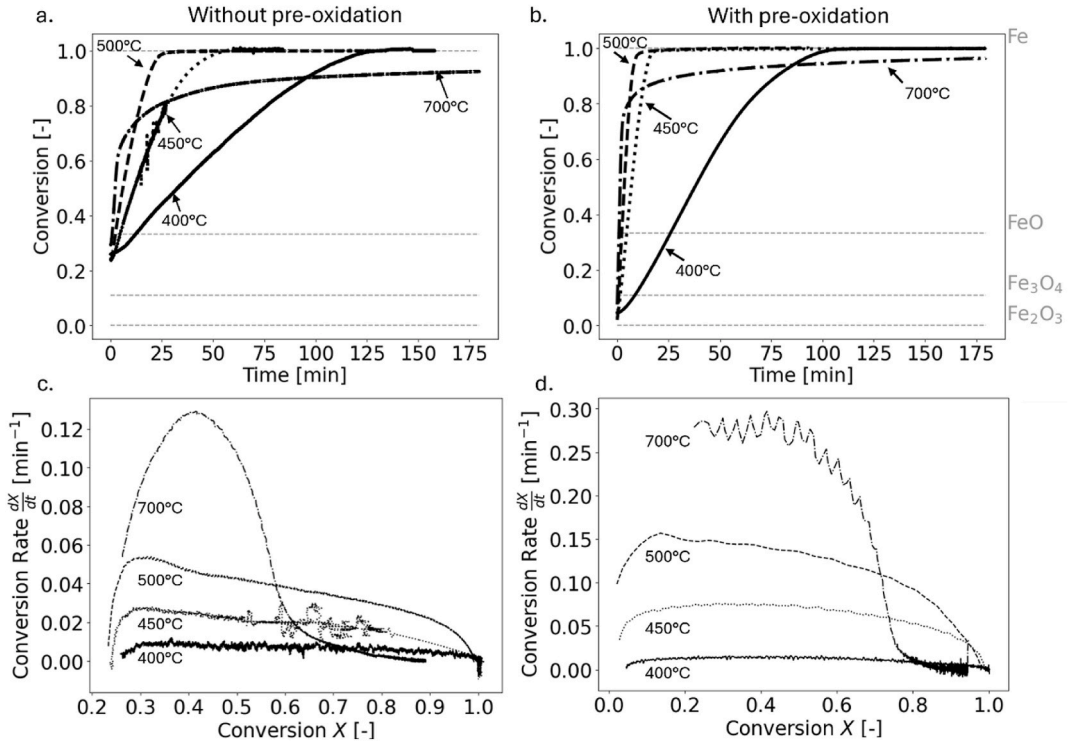

Fig. 4. Reduction kinetics measured by thermogravimetry at 400 °C - 700 °C of (a), (c) as-received and (b), (d) pre-oxidized mill-scale at 800 °C 3 h, represented by the evolution of (a), (b) conversion over time and (c), (d) conversion rate over conversion.

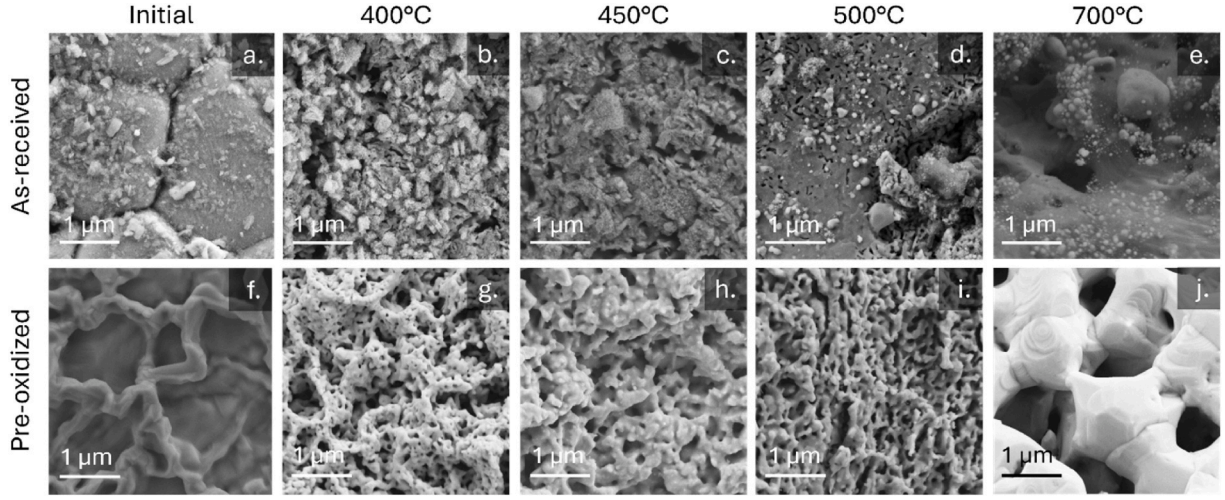

Fig. 5. Scanning Electron micrographs of the surface of initial and reduced mill scale particles at 400 °C, 450 °C, 500 °C or 700 °C for 3h with and without pre-oxidation at 800 °C for 3h (secondary electron signal).

received particles are composed of a wüstite matrix with magnetite islands that can present geometrical patterns (Fig. 9a–c). At 34% of conversion (Fig. 9d–f), metallic iron is observed at the edges of the particles and near cracks. Needles of magnetite are observed in addition to the initial blocks of magnetite (Fig. 9e), linked to wüstite decomposition studied in neutral atmosphere in the next section. As the reduction time increases, the porous phases expand towards the center of the particle (Fig. 9g). A magnetite layer is visible in between the iron and wüstite phases (Fig. 9h and i).

3.3. Wüstite decomposition under neutral atmosphere

Thermodynamically, wüstite is unstable below 570 °C. The decomposition of as-received mill scale particles (composed of more than 80 wt % of wüstite) was analyzed under nitrogen at 500 °C to decouple its decomposition from its reduction under hydrogen. The evolution over time of the XRD spectra of six samples is given in Fig. 10a and b, while the output of the quantitative analysis is provided in Fig. 10c. The initial phase proportions are given in Table 2. Hematite quickly disappears, while a strong increase in magnetite is observed. Furthermore, a change in the lattice parameter of the wüstite phase also occurs, varying between 4.26 Å and 4.31 Å, as highlighted by the shift to the left and the split into two or more peaks in the XRD spectra around 49° in Fig. 10b. The left peaks correspond to iron-enriched wüstite phases and the right ones to iron-depleted wüstite phases. Wüstite becomes more enriched in Fe in the first 1000 s, then stabilizes as iron nuclei appears. Fig. 10d

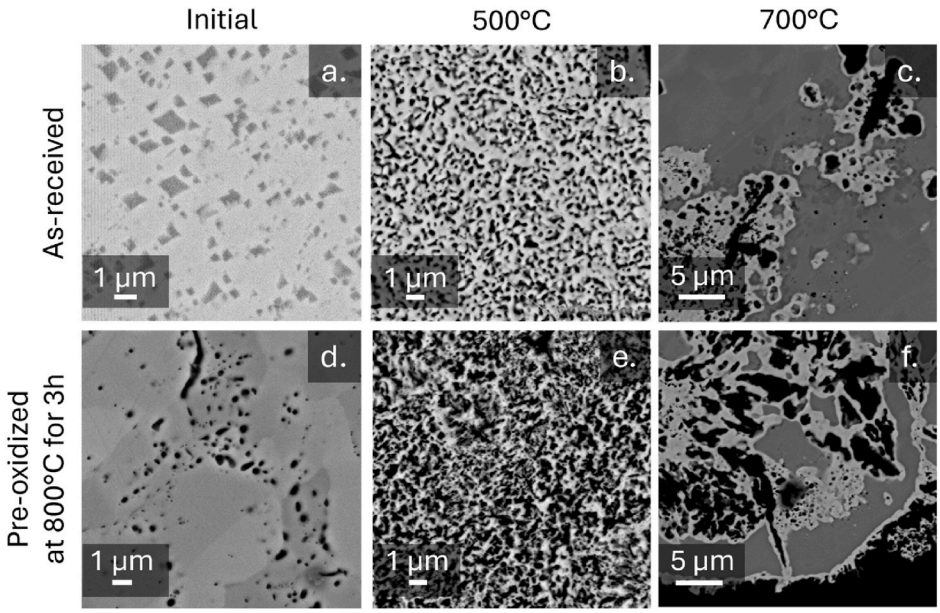

Fig. 6. Scanning Electron micrographs of the cross-section of initial and reduced mill scale particles for 3h at 500 °C or 700 °C, with and without a pre-oxidation step (backscattered electrons signal).

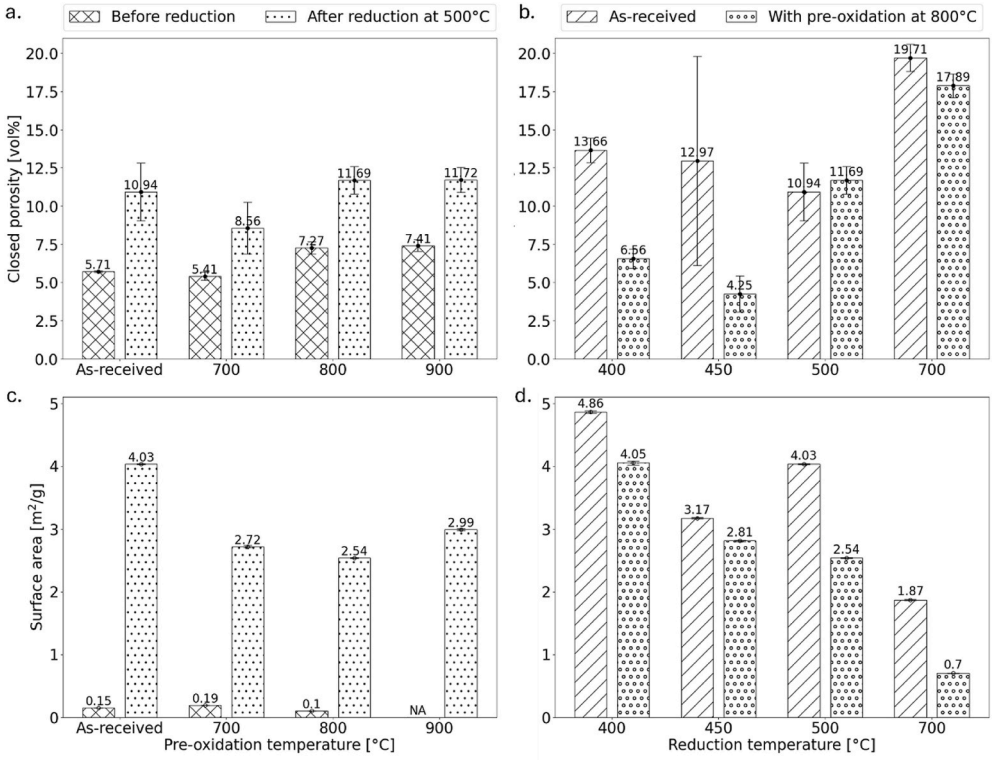

Fig. 7. Evolution of the closed, non-percolating porosity and surface area of mill scale particles, measured by nitrogen gas pycnometer and BET Krypton gas adsorption, as a function of: (a), (c) pre-oxidation temperature before and after reduction at 500 °C; (b), (d) reduction temperatures with and without pre-oxidation at 800 °C for 3h. In subfigure (c), the surface area lies below the detection limit after pre-oxidation at 900 °C. The error bars are the standard deviation over 10 measurements.

presents the evolution of the average oxygen fraction x_0 in the wüstite phase for the as-received mill scale and heat-treated samples at 500 °C for up to 3 h. After the heating period, a significant decrease in x_0 is observed: the iron content of wüstite increases, accompanied by the formation of magnetite. The remaining iron-rich wüstite will decompose into magnetite and iron afterwards.

4. Discussion

4.1. Mechanisms of reduction and decomposition

Different steps govern iron oxides reduction as a function of temperature, particularly above and below 570 °C. Hematite (highest

Table 3
Composition of the initial/oxidized and partially reduced samples at 500 °C with and without pre-oxidation at 800 °C. The first column gives the duration of the reduction experiment, and the second one gives the obtained conversion degree X for the corresponding sample. In the case with pre-oxidation, the initial sample corresponds to the one oxidized at 800 °C for 3h.

	Reduction time [s]	Obtained conversion X [−]	Hematite [wt %]	Magnetite [wt %]	Wüstite [wt %]	Iron [wt %]
With preox.	0	0.03	83.1	16.9	0	0
	30	0.08	71.8	23.8	0	4.4
	100	0.20	42.6	41.3	0	16.1
	390	0.65	0	46.7	0	53.3
Without preox.	0	0.25	2.6	16.0	81.4	0
	42	0.34	0	39.0	51.1	9.9
	980	0.95	0	2.1	4.6	93.3

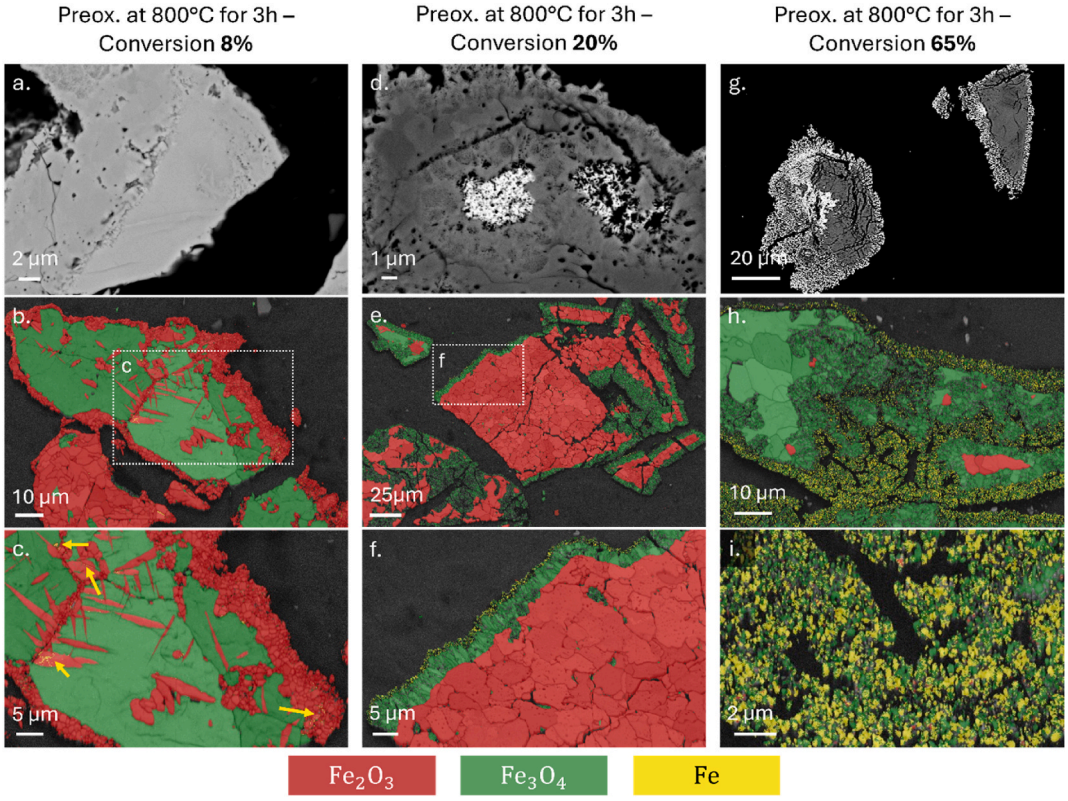

Fig. 8. Scanning Electron micrographs of the cross-section of pre-oxidized mill scale particles, partially reduced at 500 °C up to 8% (a-c), 20% (d-f) and 65% (g-i) conversion. (a), (d) and (g) electron backscattered contrast; (b-c), (e-f) and (h-i) electron backscatter diffraction (EBSD). The yellow arrows in (c) highlight the presence of iron. (For interpretation of the references to colour in this figure legend, the reader is referred to the Web version of this article.)

oxidation degree) is first reduced to magnetite, independently of the temperature:

$$3\,Fe_2O_3 + H_2 \rightarrow H_2O + 2\,Fe_3O_4 \quad (2)$$

Below 570 °C, magnetite is then directly reduced to metallic iron:

$$Fe_3O_4 + 4\,H_2 \rightarrow 4\,H_2O + 3\,Fe \quad (3)$$

Above 570 °C, wüstite is thermodynamically stable and is observed as an intermediate compound. Magnetite is thus first reduced to wüstite before further reduction to iron:

$$Fe_3O_4 + H_2 \rightarrow H_2O + 3\,FeO \quad (4)$$

$$FeO + H_2 \rightarrow H_2O + Fe \quad (5)$$

To these chemical reaction steps must be added the possibility of a simultaneous decomposition of unstable FeO below 570 °C. Slow wüstite decomposition was observed together with an increase in magnetite and iron in Fig. 10. Additionally, a rapid decrease in the amount of Fe_2O_3 is also observed. This could be explained by a local redistribution of oxygen towards the thermodynamically more stable phases for this low oxygen pressure and temperature, i.e. Fe_3O_4 and Fe. Yet, the hematite decrease could also result from sampling, as hematite is present in low quantities, inhomogeneously distributed among the particles (see Table 2). However, the increase in magnetite cannot be explained solely by this decrease in hematite, and the formation of Fe in neutral atmosphere proves the decomposition of wüstite.

As illustrated in Fig. 10b, wüstite gets first enriched in Fe with the nucleation of Fe_3O_4. The peaks of iron-rich wüstite then stabilize around 49.35°, with the additional formation of metallic iron. This is shown by the stabilization of the average oxygen fraction around 0.518, corresponding to the expected mole fraction for the eutectoid decomposition of wüstite based on the equilibrium phase diagram Fe–O. Consequently, a two steps mechanism of decomposition, previously proposed by Otsuka et al. [42], is observed here:

$$Fe_{1-x}O \rightarrow \frac{x-y}{1-4y}\,Fe_3O_4 + \frac{1-4x}{1-4y}\,Fe_{1-y}O \;(x \geq y) \quad (6)$$

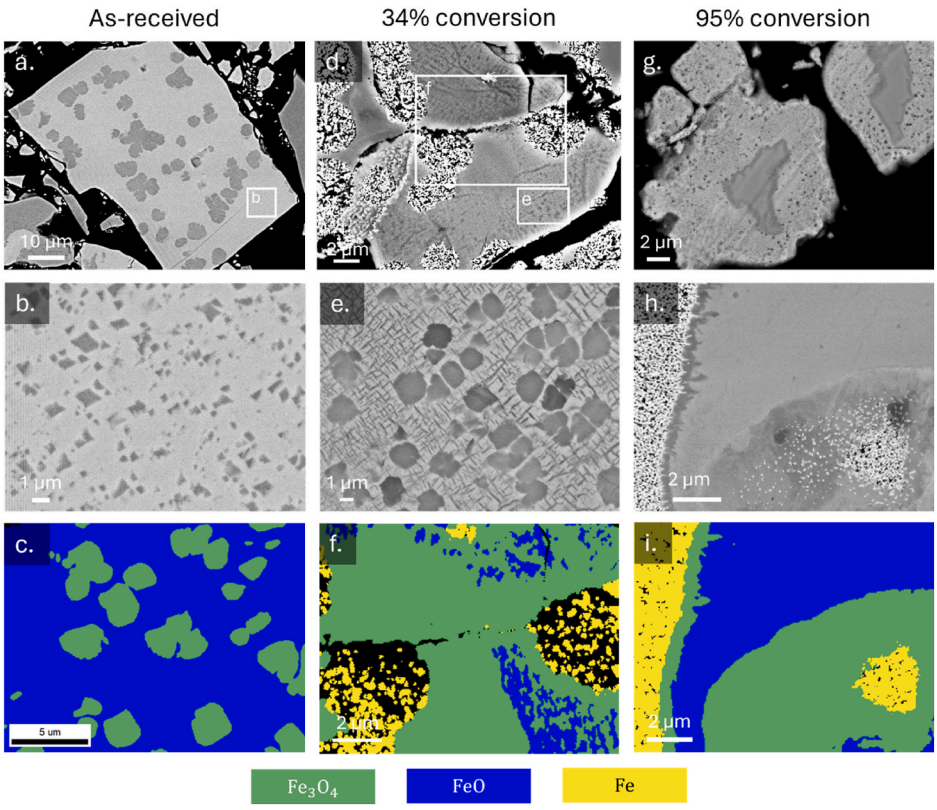

Fig. 9. Scanning Electron micrographs of the cross-section of non-pre-oxidized mill scale particles, partially reduced at 500 °C up to 0% (a-c), 34% (d-f) and 95% (g-i) conversion. (a-b), (d-e) and (g-h) electron backscattered contrast; (c), (f) and (i) electron backscatter diffraction (EBSD).

$$4\,Fe_{1-y}O\ (\text{iron rich}) \rightarrow Fe_3O_4 + (1-4y)\,Fe \quad (7)$$

Gleeson et al. [43] developed an isothermal transformation diagram for the different morphologies of wüstite (for similar mill scale to the present one) eutectoid decomposition below 570 °C under air for different holding times. Between 250 °C and 500 °C, magnetite first appears close to the wüstite/magnetite interface, prior to the iron + magnetite eutectoid decomposition. After a relatively long time (~2 h), a mix of iron and magnetite forms with a lamellar structure [43]. Eutectoid Fe/Fe_3O_4 lamellae in as-received mill scale was also observed by Guan et al. [30] and by Jie et al. [44]. In the present case, only magnetite precipitates with a block morphology (Fig. 9a–e) and no lamellar structure are observed, even after 3h at 500 °C under nitrogen atmosphere. Even though iron is detected by XRD (~3.7 wt %), iron precipitates could not be observed in the microstructure using SEM, likely because of its nanometric size.

4.2. Mill scale oxidation

An outward growth of the iron oxides is observed on the surface of pre-oxidized samples together with a small increase in closed percolating porosity (Fig. 7a). This oxide expansion is illustrated in Fig. 3d–i where a porous, crown-like layer forms around the original particle boundary. This microstructure evolution can be explained by the faster diffusion of iron cations towards the external surface (interface between iron oxides and air) compared to the diffusion of oxygen anions towards the center of the particle [45]. The migration of iron cations towards the surface leaves behind vacancies and closes surface pores, increasing the content of non-percolating porosity. Depending on the oxidation temperature, the final appearance of the porous surface is different. At 700 °C, the porous angular structure (Fig. 3a) could originate from preferential growth of hematite in favored directions, as previously reported by Zheng et al. [45], slightly increasing the specific surface area of the powder. At larger temperatures, smoothing of the surface of the particles leads to a decreased surface area. The latter is driven by the decrease in the internal energy of the system and the accelerated ionic diffusion with temperature. Strong delamination is also highlighted at the initial boundaries of the particles, between the outer scale (from strong outward diffusion of iron cations) and inner oxidation of the surface mill scale particle (from weak inward diffusion of oxygen anions) (Fig. 3d). The accumulation of vacancies at this boundary, due to the strong local ionic diffusion and change in defects density, causes the formation of microcracks and eventual delamination upon local stresses, as reported during iron oxidation by Mitchell et al. [46].

Reduction at 500 °C is faster with a pre-oxidation at 800 °C, as illustrated in Fig. 2. This can be explained by the microstructural changes described above. During oxidation at 700 °C, complete oxidation of the mill scale is not achieved (as described in Section 3.1) and the presence of remaining magnetite slows down the subsequent reduction. At 900 °C, diffusion is more active, and the outer layer is much denser than at 800 °C, which will block the diffusion of hydrogen within the particles during reduction.

4.3. Mill scale reduction

Reduction process can be described by multiple models based on the limiting kinetic mechanism. 3 models are compared here, consistent with the literature [40,47].

- Phase-boundary-controlled model (PBC): also known as core shell or heterogeneous shrinking-core model, this model considers spherical particles. The slowest step, limiting the reaction kinetics, is the reduction reaction at the boundary between the reactant phase (core, which has not yet reacted) and the product phase (present in the shell).

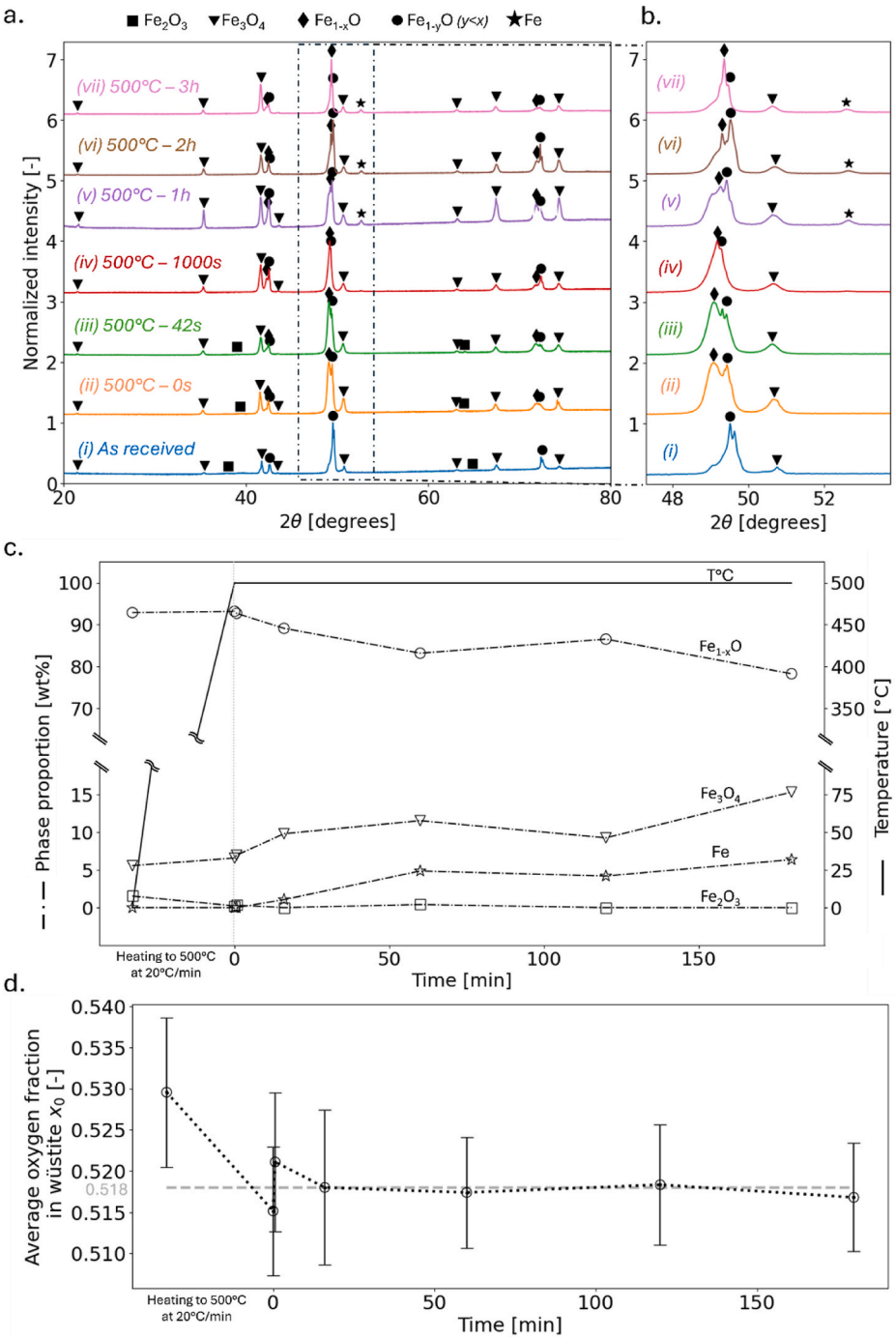

Fig. 10. X-ray diffraction analysis of the decomposition of wüstite. (a) and (b) XRD spectra of (i) initial mill scale particles and after (ii) 0 s, (iii) 42 s, (iv) 1000 s, (v) 1 h, (vi) 2 h and (vii) 3 h at 500 °C. Evolution of (c) the phase proportion and (d) the average oxygen fraction in wüstite over time, from Rietveld refinement of the XRD spectra. The propagation of error rule is used to estimate the error bar presented.

- Internal diffusion model (Diff): is a model limited by the diffusion of reactants through the reaction medium. The reaction rate will be equal to that of the transport of the reactants through the oxides or of the products through the reduced layer.
- Nucleation and growth model (NAG): it is assumed that the nucleation of the reduced phase and its growth from the reaction phase will limit the reaction kinetics. The interactions between the initial phase and newly nucleated one are described by the Avrami equation. This equation involves a parameter *n* (between 1 and 4), known as the order of the model or the Avrami exponent, which depends on both the assumptions made about the nucleation mechanism (random or non-random nucleation, presence of preferential sites, etc.) and the dimensionality of the nuclei growth (1D, 2D or 3D).

With each theoretical model, a mathematical expression for the evolution of the conversion is given [47] (see Supplementary Table S1). To quantify the kinetics parameters of the reactions, kinetic fitting was performed on the evolution of the conversion from the TGA (Fig. 4b) based on these models. The mathematical developments and methods for this kinetic analysis are given in Supplementary Material (Supplementary Figs. S6, S7 and S8). To estimate the error propagation, a resampling of the data has been applied a thousand times following a

bootstrap method (further explained in Supplementary Materials).

4.3.1. Direct hydrogen reduction below 570 °C

4.3.1.1. With pre-oxidation. Pre-oxidation (at 700 °C, 800 °C or 900 °C) always accelerates the subsequent reduction reaction, irrespective of the reduction temperature (between 400 and 700 °C), as shown in Figs. 2 and 4. 800 °C for 3 h was chosen as the best pre-oxidation treatment for the rest of this work as it gave the highest subsequent reduction rate at 500 °C.

When oxidation is carried out prior to the reduction, mill scale only consists of magnetite and hematite. Below 570 °C, hematite reduction occurs in two steps, assumed to evolve simultaneously: (i) reduction of hematite to magnetite, and (ii) reduction of magnetite to metallic iron:

$$(i)\ 3Fe_2O_3 + H_2 \rightarrow 2Fe_3O_4 + H_2O \quad (8)$$

$$(ii)\ Fe_3O_4 + 4H_2 \rightarrow 3Fe + 4H_2O \quad (9)$$

The reduction of hematite and magnetite (mostly present in pre-oxidized samples) is therefore faster than for wüstite (predominant in as-received particles). This analysis is also supported by Wolfinger et al. [32], who analyzed the impact of pre-oxidation on the direct reduction of magnetite at 800 °C – 1000 °C and found that a higher degree of oxidation favors the reduction rate.

Regarding microstructure and morphologies evolution, no significant changes in porosity are observed at the surface of the particles (Fig. 5e-f-g) with the temperature of reduction (400 °C, 450 °C or 500 °C). Pre-oxidation consistently leads to a smaller closed porosity content after reduction compared to the reduced particles without pre-oxidation, as shown in Fig. 7b. This decrease could be due to better connectivity of the internal pores with the surface, thus reducing the closed volume of porosity. An increase in the surface area would therefore be expected. However, the opposite trend is observed (Fig. 7d). This can be explained by an increase in the size of the pores at the surface, as illustrated in Fig. 5. As the surface-to-volume ratio of a sphere or cylinder is inversely proportional to the radius, the increase in volume involves a decrease in surface area, compensating the better connectivity with the internal pores.

In Fig. 8b and c, reduction of both Fe_2O_3 and Fe_3O_4 is observed to occur simultaneously in a zone of about 20 μm in depth, as previously observed for the reduction of pure iron oxides particles in the same temperature range [40]. Hematite reduction occurs towards the center in a concentric way, suggesting a core shell limiting mechanism. Pre-oxidation leads to a higher hematite content, which is then rapidly reduced. This reduction leads to an increase in the amount of magnetite produced. In Fig. 8d, iron is nucleating and then growing in such pores but also around defects (i.e. cracks, grain boundaries). These observations can be linked to a nucleation and growth model for the reduction of porous magnetite coming from the hematite reduction. The increase in porosity from hematite reduction leads to an increase in specific surface area which allows for a larger diffusion path for hydrogen. These wider channels generate a decrease in internal transport resistance, which accelerates the reduction kinetics observed in Figs. 2 and 4. On the other hand, initial dense magnetite, not originating from Fe_2O_3 reduction, is also observed in the center of the particles (Fig. 8g and h), suggesting a final phase boundary mechanism. This sequence of models (phase boundary for hematite reduction and nucleation and growth for magnetite reduction) was also the conclusion of Choisez et al. [40] for pre-oxidized pure iron particles reduced at 400°C-500 °C under H_2 based on microstructure observations and a similar kinetic study. The presence of additional impurities and different morphology of the mill-scale powder do not affect the dominant mechanisms of direct reduction in the 400°C-500 °C range.

Kinetic fitting was then used to confirm the limiting mechanism suggested based on the microstructure evolution observations. Supplementary Fig. S6 illustrates the results of the fits for a phase boundary mechanism followed by a nucleation and growth process, the two previously chosen models. The R-squared values are available for all models in Table S2 in Supplementary Materials. The apparent activation energy and pre-exponential factor for both hematite and magnetite reduction was then derived from fitted rate constants, from Arrhenius equation $k = k_0 \cdot \exp\left(-\frac{E_a}{RT}\right)$, given in Table 4 and Supplementary Fig. S8. An increase in the rate constants is observed with increasing temperature, as expected based on Arrhenius equation. For magnetite reduction, the Avrami exponents are close to 2, typically corresponding to a surface nucleation with one-dimensional growth, similar to the H_2 reduction of pure iron oxide powder by Choisez et al. [40]. Both obtained apparent activation energies are consistent with literature: 119 kJ/mol for the reduction of hematite to magnetite with reported values around [76;140] kJ/mol [40,47,48,51] and 105 kJ/mol for magnetite reduction to iron with reported values around [52; 186] kJ/mol [33,40,48–50]. As the apparent activation energy depends on a large number of different parameters (raw material, nature of the reducing gas, temperature range, reaction stages, impurities, etc.) [48], it is not surprising to find wide variations between the different values available in the literature. Comparative tables (Tables S3 and S4) of apparent activation energies with experimental conditions are available as Supplementary Material for both hematite and magnetite reduction. Finally, the rate-limiting step of the whole reduction process at temperatures below 570 °C, is the reduction of magnetite to iron, as shown by the microstructural analysis and the lower rate constant.

4.3.1.2. Without pre-oxidation. In the case without pre-oxidation, four reactions can be considered: (i) reduction of hematite to magnetite, (ii) reduction of magnetite to iron, (iii) reduction of wüstite to iron and (iv) decomposition of wüstite into magnetite and iron:

$$(i)\ Fe_2O_3 + H_2 \rightarrow Fe_3O_4 + H_2O \quad (11)$$

$$(ii)\ Fe_3O_4 + 4H_2 \rightarrow 3Fe + 4H_2O \quad (12)$$

$$(iii)\ FeO + H_2 \rightarrow Fe + H_2O \quad (13)$$

$$(iv)\ 4FeO \rightarrow Fe_3O_4 + Fe \quad (14)$$

The first reaction occurs quickly during the heating step (Fig. 10c) due to the low initial Fe_2O_3 content (~2.5 wt %, Fig. 1) and high reactivity. The major part of reduction of hematite at the start of the reaction is also noted in the literature [40,48,51]. As for the case with pre-oxidation, the second reaction seems to be first governed by nucleation and growth (NAG) of iron, with favored nucleation sites in porous Fe_3O_4 (edge) and on defects (cracks and grain boundaries) (Fig. 9d). At the end, a core shell mechanism is also suggested from Fig. 10g, with a magnetite layer surrounding dense wüstite in the center. These oxidized islands reduce towards the center of the particle. As the thickness of the magnetite layer seems to stay constant, the production and the disappearance of magnetite occur at approximately the same rate. Reactions (iii) and (iv) are more difficult to decorrelate, as both consume FeO to form Fe. Since magnetite reduction is reported to be easier and faster than for wüstite [52–54] and considering that a magnetite layer is always present between the wüstite and iron phase, even for large reduction levels (95%) (Fig. 9h and i)), the decomposition of wüstite (iii) appears to be dominant compared to its direct reduction (iv). Wüstite first decomposes into magnetite according to Equation (6) and magnetite is then directly reduced to iron due to the reducing atmosphere. Wüstite decomposition is also favored by the presence of a reducing agent by Le Chatelier. Indeed, after 1000 s without hydrogen, a decrease of 10 wt % of wüstite is noted (Fig. 10c) whereas, in the presence of reducing agent for the same duration, wüstite has almost completely disappeared (Table 3). Wüstite eutectoid decomposition could be limited by a diffusion mechanism (Diff) as there is a redistribution of oxygen ions. Large variations in the size of the crystalline lattice are

Table 4
Kinetic parameters (rate constant, Avrami exponent, apparent activation energy, pre-exponential factor) for hematite to magnetite and magnetite to iron reductions, fitted using PBC and NAG models, respectively.

		400	450	500
Reduction of hematite to magnetite (PBC)	Rate constant [min^{-1}]	$33.69 \cdot 10^{-3} \pm 244 \cdot 10^{-3}$	$248.46 \cdot 10^{-3} \pm 71.44 \cdot 10^{-3}$	$513.03 \cdot 10^{-3} \pm 260.4 \cdot 10^{-3}$
	Apparent activation energy [kJ/mol]	118.91		
	Pre-exponential factor [min^{-1}]	$67.27 \cdot 10^{6}$		
Reduction of magnetite to iron (NAG)	Rate constant [min^{-1}]	$19.63 \cdot 10^{-3} \pm 0.0114 \cdot 10^{-3}$	$109.70 \cdot 10^{-3} \pm 0.18 \cdot 10^{-3}$	$215 \cdot 10^{-3} \pm 0.53 \cdot 10^{-3}$
	Avrami exponent n [−]	1.86 ± 0.011	1.88 ± 0.011	1.69 ± 0.01006
	Apparent activation energy [kJ/mol]	104.59		
	Pre-exponential factor [min^{-1}]	$2.941 \cdot 10^{6}$		

indeed observed, as illustrated in Fig. 10 and developed in Section 4.1. Another possibility would be for the eutectoid decomposition to be controlled by a nucleation and growth model (NAG). Indeed, during wüstite decomposition, iron nucleation is observed to be very slow, while and magnetite increases from the start (Fig. 10). Moreover, magnetite will precipitate from oxygen-rich wüstite and the limiting factor for precipitation can be the nucleation and growth of iron phase, as described in the literature [55–57]. In conclusion, both models (Diff or NAG) are possible for wüstite decomposition, while a nucleation and growth mechanism (NAG) for magnetite reduction is chosen to compute the apparent activation energy.

The results of the kinetic fitting are given in Supplementary Fig. S7. Quantitative data are only given considering a diffusion model for the wüstite decomposition as it gives, at all temperatures, higher R-squared values than considering a nucleation and growth mechanism (see Table S2 in Supplementary Materials). The associated rate constant (and Avrami exponent) at each temperature, the apparent activation energy and pre-exponential factor for the reaction are summarized in Table 5 and the Arrhenius plots are given in Supplementary Fig. S8. As the Avrami exponents are close to 1, magnetite reduction is solely limited by the nucleation itself. The apparent activation energy of magnetite lies in the range of the literature, as shown above in the case with pre-oxidation (Section 4.3.1.1 or Table S3). For the apparent activation energy of wüstite decomposition, no results are found in the literature. Finally, the rate-limiting step of the whole reduction process at temperatures below 570 °C is the eutectoid decomposition of wüstite has developed previously with the microstructural analysis and shown by lower rate constants.

In conclusion, Table 6 shows a comparison of both reduction pathways under 570 °C. In the case with pre-oxidation, reduction happens in two steps. First, hematite is reduced to magnetite following a phase boundary mechanism. The subsequent reduction of magnetite to iron is limited by a nucleation-and-growth mechanism. Dense magnetite can also be present when the initial sample is not fully pre-oxidized. The reduction of dense magnetite is controlled by a phase boundary mechanism. On the other hand, without pre-oxidation, the scheme is more complex and is summarized in Table 6. Firstly, the traces of hematite quickly disappear without a clear limitation of the reaction kinetics. Eutectoid wüstite decomposition is then predominant and could be limited by a nucleation and growth or diffusion mechanism. Wüstite

Table 6
Comparison of hydrogen-based direct reduction of as received and pre-oxidized mill scale below 570 °C.

With pre-oxidation	Without pre-oxidation
1. $3Fe_2O_3 + H_2 \rightarrow 2Fe_3O_4 + H_2O$ ⇨ Limited by PBC	1. $3Fe_2O_3 + H_2 \rightarrow 2Fe_3O_4 + H_2O$ ⇨ Not limiting the reaction
2. $Fe_3O_4 + 4H_2 \rightarrow 3Fe + 4H_2O$ ⇨ Limited by NAG when porous, i.e. arising from Fe_2O_3 ⇨ Limited by PBC when dense, i.e. initially present	2. $FeO \rightarrow Fe_3O_4 + Fe$ ⇨ Limited by Diff or NAG ⇨ Promoted by the presence of a reducing agent
	3. $Fe_3O_4 + 4H_2 \rightarrow 3Fe + 4H_2O$ ⇨ Globally limited by NAG ⇨ In final stage, limited by PBC

decomposition is strongly promoted by the presence of a reducing agent. Finally, magnetite is reduced into $\alpha-$ iron. This reduction step is globally controlled by a nucleation and growth mechanism, but, in the final stage, a phase boundary mechanism is observed.

4.3.2. *Direct hydrogen reduction at 700 °C*

At 700 °C, the reduction follows a three steps mechanism: (i) reduction of hematite to magnetite, (ii) reduction of magnetite to wüstite and (iii) reduction of wüstite to iron. The formation and reduction of this intermediate wüstite could slow down the overall reaction, as observed for reductions below 570 °C (Subsection 4.3.1.). As illustrated in Fig. 4, pre-oxidation increases not only the reduction rate but also the level of stabilization of the conversion degree. Reduction kinetics is favored by the disappearance of the wüstite phase and the appearance of the hematite phase where the oxygen ion diffusion is highest. On the other hand, the stabilization level can have two origins: (1) the transition to external gas diffusion limitation due to interparticle sintering or (2) ionic diffusion limitation due to dense iron layer formation. The first hypothesis was discarded as an open network could be observed in between the particles of the agglomerate collected after reduction at 700 °C for 3 h, using X-ray computed tomography (Fig. S5 in Supplementary Material). The second hypothesis was confirmed by microstructural analysis (Fig. 5b and d), where several islands of wüstite are surrounded by a dense iron layer. A similar limitation was previously reported during iron oxides reduction at 700 °C in hydrogen and was associated to the faster Fe ionic diffusion at that temperature, decreasing

Table 5
Kinetic parameters (rate constant, Avrami exponent, apparent activation energy, pre-exponential factor) for wüstite decomposition and magnetite to iron reduction, fitted using Diff and NAG models, respectively.

		400	450	500
Decomposition of wüstite into magnetite and iron (Diff)	Rate constant [min^{-1}]	$7.47 \cdot 10^{-3} \pm 0.023 \cdot 10^{-3}$	$18.87 \cdot 10^{-3} \pm 0.18 \cdot 10^{-3}$	$36.04 \cdot 10^{-3} \pm 0.084 \cdot 10^{-3}$
	Apparent activation energy [kJ/mol]	68.27		
	Pre-exponential factor [min^{-1}]	$1.521 \cdot 10^{3}$		
Reduction of magnetite to iron (NAG)	Rate constant [min^{-1}]	$18.14 \cdot 10^{-3} \pm 0.043 \cdot 10^{-3}$	$51.73 \cdot 10^{-3} \pm 0.17 \cdot 10^{-3}$	$100.76 \cdot 10^{-3} \pm 0.15 \cdot 10^{-3}$
	Avrami exponent n [−]	1.37 ± 0.016	1.29 ± 0.011	1.29 ± 0.0038
	Apparent activation energy [kJ/mol]	74.45		
	Pre-exponential factor [min^{-1}]	$11.306 \cdot 10^{3}$		

porosity in reduced Fe [58–60]. The formation of this denser layer can entrap a larger volume of porosity (explaining the higher closed volume of porosity observed in Fig. 7b), while strongly decreasing the surface area (Fig. 7d).

As presented in Fig. 5d and h, the particle surface after reduction is significantly different when applying pre-oxidation. Without the prior oxidation step, the surface is very irregular, and numerous bubbles are present on it. This is probably due to the presence of numerous elements other than Fe present in small amount that cannot be reduced using hydrogen (Al, Si, Ca …), changing the morphology to spherical to decrease the internal energy and interfaces. Further investigations are yet needed to confirm this hypothesis. In the case with pre-oxidation, wide pores were noted (Fig. 5h). These largest pores appear to be growing in layers. El-Rahaiby *et* Rao [61] also observed a similar trend for the formation of wüstite. The observed structure could therefore result from the formation of wüstite by magnetite reduction.

4.3.3. Process improvements

From the understanding of previous mechanisms, a few conclusions can be drawn to improve the industrial reduction process. Mill scale is abundant, but a non-negligible amount is still treated as a waste. The latter could be valorized as sustainable energy carriers [9,10], using hydrogen-based direct reduction of the fines in fluidized bed reactors. The following insights can be concluded from our work. The direct reduction at 700 °C should be avoided to avoid the formation of a diffusion-limiting, dense iron layer. The addition of a pre-oxidation step at 800 °C accelerates the reduction kinetics. This pre-oxidation step can be even more energetically interesting if the heat from the oxidation of the mill scale is valorized, *e.g.,* to heat the reaction gas. However, the direct reduction of the initial mill scale without pre-oxidation might be favorable if the limiting resource is hydrogen gas. Indeed, a neutral treatment could be first applied to decompose wüstite into magnetite and iron. The magnetite phase can subsequently be reduced using limited quantities of hydrogen as its reduction rate is higher than that of wüstite. Below 570 °C, two mechanisms may be limiting the reduction reaction according to our analysis: (1) nucleation and growth of iron and/or (2) ionic diffusion during wüstite decomposition. Further increase of the efficiency of the process could be brought by creating a higher density of crystalline defects to form more nucleation sites and accelerate ionic diffusion. For example, energetic mechanical debonding of mill scale from the steel slab, additional ball-milling, or optimized pre-oxidation treatment could be applied. By applying a longer pre-oxidation treatment at lower temperature, the formation of smaller grains with high specific surface area could be obtained. The overall energetic and hydrogen consumption associated with these different treatments should be evaluated to optimize the overall recycling process. Further work on a larger scale is required to assess the impact of the different process parameters on the reduction efficiency of mill scale powder fines in fluidized bed reactors. Nevertheless, the identification of the fundamental mechanisms governing the reduction reaction at the particle scale in this work can serve as a guide for the following process-scale analyses.

5. Conclusion

This work evaluates the feasibility of recycling industrial mill scale fines using HyDR as a potential sustainable source of iron. The reduction behavior of mill scale powder, mainly constituted of wüstite, was investigated at low temperatures (400 °C, 450 °C, 500 °C and 700 °C) under pure H_2 using a thermogravimetric analyzer (TGA) and microstructural analysis. The influence of pre-oxidation at 700 °C – 900 °C was also investigated. Pre-oxidation consistently accelerated the subsequent reduction at all investigated temperatures. Among the tested conditions, pre-oxidation at 800 °C resulted to the fastest subsequent reduction at 500 °C. At 700 °C, reduction is ultimately limited by the formation of a dense iron layer surrounding unreduced wüstite islands. In this temperature regime, pre-oxidation also increases the final stabilized conversion degree from 92 to 95% after 3 h of reduction.

At intermediate temperatures (400 °C, 450 °C and 500 °C), distinct mechanisms were identified depending on the state of the initial oxidation. For pre-oxidized particles, hematite to magnetite reduction follows a phase boundary mechanism (with an apparent activation energy of 118.9 kJ/mol), while the simultaneous reduction of magnetite to iron is limited by a surface nucleation and one-dimensional growth model (with an apparent activation energy of 104.6 kJ/mol). Microstructural observations confirmed that hematite reduction is fast, whereas iron nucleation from magnetite is the rate-limiting step.

Without pre-oxidation, the initial presence of wüstite introduces additional reaction pathways. Wüstite decomposition occurs simultaneously with magnetite to iron reduction, leading to more complex kinetics. Magnetite reduction is limited by the nucleation of metallic iron with an apparent activation energy of 74.45 kJ/mol. The eutectoid decomposition of wüstite into magnetite and iron may be controlled either by a nucleation and growth or by a diffusion mechanism. The latter provides the best kinetic fit and has an associated apparent activation energy of 68.27 kJ/mol. Complementary experiments conducted in a neutral atmosphere further demonstrated a two-steps wüstite decomposition mechanism: initially enriching wüstite in iron, followed by its decomposition into magnetite and iron precipitates. The latter constitutes the rate-limiting step of this reaction.

Hydrogen-based direct reduction of mill scale fines is technically feasible in the 400 °C – 500 °C range, with pre-oxidation playing a key role in accelerating reduction kinetics and modifying the dominant reaction mechanisms. This study supports the potential of mill scale as an alternative and sustainable iron source within hydrogen-based ironmaking routes.

CRediT authorship contribution statement

Bénédicte Kuypers: Writing – original draft, Visualization, Software, Investigation, Formal analysis. **Nicole C. Stevens:** Writing – review & editing. **Conrad J.M. Hessels:** Writing – review & editing. **Pascal J. Jacques:** Writing – review & editing, Supervision, Resources. **Giulia Finotello:** Writing – review & editing, Supervision, Resources, Conceptualization. **Laurine Choisez:** Writing – review & editing, Supervision, Methodology, Conceptualization.

Declaration of competing interest

The authors declare that they have no known competing financial interests or personal relationships that could have appeared to influence the work reported in this paper.

Acknowledgments

We thank for their support the chemical lab, metallography lab, XRD and SEM facilities at UCLouvain (especially the LACAMI laboratory) and TU Eindhoven. LC acknowledges financial support through F.R.S.-FNRS chargée de recherche mandate.

Appendix A. Supplementary data

Supplementary data to this article can be found online at https://doi.org/10.1016/j.ijhydene.2026.154185.

Data availability

The datasets generated during and/or analyzed during the current study are available from the corresponding author on reasonable request.

References

[1] IEA. Iron and steel technology roadmap – analysis. Paris: IEA; 2020.
[2] Ariyama T, Sato M, Nouchi T, Takahashi K. Evolution of blast furnace process toward reductant flexibility and carbon dioxide mitigation in steel works. ISIJ Int 2016;56:1681–96.
[3] Jin P, Jiang Z, Bao C, Hao S, Zhang X. The energy consumption and carbon emission of the integrated steel mill with oxygen blast furnace. Resour Conserv Recycl 2017;117:58–65.
[4] Ma Y, Souza Filho IR, Bai Y, Schenk J, Patisson F, Beck A, Van Bokhoven JA, Willinger MG, Li K, Xie D, et al. Hierarchical nature of hydrogen-based direct reduction of iron oxides. Scr Mater 2022;213:114571.
[5] Jikar PC, Dhokey NB. Overview on production of reduced iron powder from mill scale waste. Mater Today Proc 2021;44:4324–9.
[6] Taylor B. Global steel output down slightly in 2024. Recycl Today 2025. https://www.recyclingtoday.com/news/worldsteel-2024-production-global-turkey-india-recycling/.
[7] Bergthorson JM, Goroshin S, Soo MJ, Julien P, Palecka J, Frost DL, Jarvis DJ. Direct combustion of recyclable metal fuels for zero-carbon heat and power. Appl Energy 2015;160:368–82.
[8] Choisez L, Hessels CJM, Hermanns RTE, Jacques PJ. Iron as a sustainable energy carrier. Nat Rev Mater 2025:1–3.
[9] Choisez L, Stevens N, Prasidha W, Kuypers B, Mauxion T, de Goey P, Finotello G, Jacques PJ. On the use of industrial steel mill scale as a high-density energy carrier: part I. Reaction processes and particle size evolution over cycling. Fuel 2026;405:136614.
[10] Choisez L, Kuypers B, Stevens N, Prasidha W, Mauxion T, de Goey P, Finotello G, Jacques PJ. On the use of industrial steel mill scale as a high-density energy carrier: part II. Microstructural and chemical evolution over cycling. Fuel 2026;406:136906.
[11] Benchiheub O, Mechachti S, Serrai S, Khalifa MG. Elaboration of iron powder from mill scale. J Mater Environ Sci 2010;1:267–76.
[12] Martín MI, López FA, Torralba JM. Production of sponge iron powder by reduction of rolling mill scale. Ironmak Steelmak 2012;39:155–62.
[13] Park J-W, Ahn J-C, Song H, Park K, Shin H, Ahn J. Reduction characteristics of oily hot rolling mill sludge by direct reduced iron method. Resour Conserv Recycl 2002;34:129–40.
[14] El-Hussiny NA, Shalabi MEH. A self-reduced intermediate product from iron and steel plants waste materials using a briquetting process. Powder Technol 2011;205:217–23.
[15] Bagatini MC, Zymla V, Osório E, Vilela ACF. Characterization and reduction behavior of mill scale. ISIJ Int 2011;51:1072–9.
[16] Eissa M, Ahmed A, El-Fawkhry M. Conversion of mill scale waste into valuable products via carbothermic reduction. Journal of Metallurgy 2015;2015:1–9.
[17] Farahat R, Eissa M, Megahed G, Baraka A. Reduction of mill scale generated by steel processing. Steel Grips 2010;8:88–92.
[18] Sen R, Dehiya S, Pandel U, Banerjee MK. Utilization of low grade coal for direct reduction of mill scale to obtain sponge iron: effect of reduction time and particle size. Procedia Earth and Planetary Science 2015;11:8–14.
[19] Yucel O, Demirci F, Turan A, Alkan M. Determination of direct reduction conditions of mill scale. High Temp Mater Process 2013;32:405–12.
[20] Joshi C, Dhokey NB. Study of kinetics of mill scale reduction: for PM applications. Trans Indian Inst Met 2015;68:31–5.
[21] Gidikova N, Manolov V, Petkov V, Valov R, Stanev S. Mill scale reduction. J Mater Sci Technol 2017;25:12–9.
[22] Sista KS, Dwarapudi S, Nerune VP. Direct reduction recycling of mill scale through iron powder synthesis. ISIJ Int 2019;59:787–94.
[23] Alghtani AH, Alsharef M, El-Aziz Kh A. Characterization of iron powder produced by reduction of hot-rolled mill scale in hydrogen gas. Mat Res 2022;25:e20210575.
[24] Gaballah NM, Zikry AF, Khalifa MG, Farag AB, El-Hussiny NA, Shalabi MEH. Production of iron from mill scale industrial waste via hydrogen. OJINM 2013;3:23–8.
[25] Elsadek M, Mousa E, Ahmed H. Green approach to ironmaking: briquetting and hydrogen reduction of mill scale using novel binders. Int J Hydrogen Energy 2024;62:732–8.
[26] Paizullakhonov MS, Abduraimov S, Kovtun O, Volkova O, Abduraimov S. Study on changes in pore size on single powder and reduction swelling index during the reduction of iron mill scale with hydrogen and forming gas. HTM; 2025. p. 29.
[27] Yi L, Huang Z, Jiang T, Wang L, Qi T. Swelling behavior of iron ore pellet reduced by H2–CO mixtures. Powder Technol 2015;269:290–5.
[28] Bonalde A, Henriquez A, Manrique M. Kinetic analysis of the iron oxide reduction using hydrogen-carbon monoxide mixtures as reducing agent. ISIJ Int 2005;45:1255–60.
[29] Zhong Y-W, Wang Z, Gong X-Z, Guo Z-C. Sticking behavior caused by sintering in gas fluidisation reduction of haematite. Ironmak Steelmak 2012;39:38–44.
[30] Guan C, Li J, Tan N, He Y-Q, Zhang S-G. Reduction of oxide scale on hot-rolled steel by hydrogen at low temperature. Int J Hydrogen Energy 2014;39:15116–24.
[31] Zheng H, Daghagheleh O, Wolfinger T, Taferner B, Schenk J, Xu R. Fluidization behavior and reduction kinetics of pre-oxidized magnetite-based iron ore in a hydrogen-induced fluidized bed. Int J Miner Metall Mater 2022;29:1873–81.
[32] Wolfinger T, Spreitzer D, Zheng H, Schenk J. Influence of a prior oxidation on the reduction behavior of magnetite iron ore ultra-fines using hydrogen. Metall Mater Trans B 2022;53:14–28.
[33] Pineau A, Kanari N, Gaballah I. Kinetics of reduction of iron oxides by H2: part II. Low temperature reduction of magnetite. Thermochim Acta 2007;456:75–88.
[34] Kim W-H, Lee S, Kim S-M, Min D-J. The retardation kinetics of magnetite reduction using H2 and H2–H2O mixtures. Int J Hydrogen Energy 2013;38:4194–200.
[35] Edström J. The mechanism of reduction of iron oxides. Journal of the Iron and Steel Institute 1953;175:289.
[36] Wang Z, Zhang J, Jiao K, Liu Z, Barati M. Effect of pre-oxidation on the kinetics of reduction of ironsand. J Alloys Compd 2017;729:874–83.
[37] Cornell, R. M., Schwertmann, U., The iron oxides: structure, properties, reactions, occurences and uses, second ed. Weinheim: Wiley-VCH.
[38] Coenen K, Gallucci F, Cobden P, Van Dijk E, Hensen E, Van Sint Annaland M. Chemisorption working capacity and kinetics of CO 2 and H 2 O of hydrotalcite-based adsorbents for sorption-enhanced water-gas-shift applications. Chem Eng J 2016;293:9–23.
[39] Zheng H, Spreitzer D, Wolfinger T, Schenk J, Xu R. Effect of prior oxidation on the reduction behavior of magnetite-based iron ore during hydrogen-induced fluidized bed reduction. Metall Mater Trans B 2021;52:1955–71.
[40] Choisez L, Hemke K, Özgün Ö, Pistidda C, Jeppesen H, Raabe D, Ma Y. Hydrogen-based direct reduction of combusted iron powder: deep pre-oxidation, reduction kinetics and microstructural analysis. Acta Mater 2024;268:119752.
[41] Berthon J, Revcolevschi A, Morikawa H, Touzelin B. Growth of wustite (fe1−x O) crystals of various stoichiometries. J Cryst Growth 1979;47:736–8.
[42] Otsuka N, Doi T, Hidaka Y, Higashida Y, Masaki Y, Mizui N, Sato M. In-situ measurements of isothermal wüstite transformation of thermally grown FeO scale formed on 0.048 mass% Fe by synchrotron radiation in air. ISIJ Int 2013;53:286–93.
[43] Gleeson B, Hadavi SMM, Young DJ. Isothermal transformation behavior of thermally-grown wüstite. Mater A T High Temp 2000;17:311–8.
[44] Jie S, De-ren W, Ye-dong H, Hui-bin Q, Gao W. Reduction of oxide scale on hot-rolled strip steels by carbon monoxide. Mater Lett 2008;62:3500–2.
[45] Zheng H, Schenk J, Xu R, Daghagheleh O, Spreitzer D, Wolfinger T, Yang D, Kapelyushin Y. Surface morphology and structural evolution of magnetite-based iron ore fines during the oxidation. Metall Mater Trans B 2022;53:1644–60.
[46] Mitchell TE, Voss DA, Butler EP. The observation of stress effects during the high temperature oxidation of iron. J Mater Sci 1982;17:1825–33.
[47] Hessels CJM, Homan TAM, Deen NG, Tang Y. Reduction kinetics of combusted iron powder using hydrogen. Powder Technol 2022;407:117540.
[48] Pineau A, Kanari N, Gaballah I. Kinetics of reduction of iron oxides by H2: part I. Low temperature reduction of hematite. Thermochim Acta 2006;447:89–100.
[49] Lin H-Y, Chen Y-W, Li C. The mechanism of reduction of iron oxide by hydrogen. Thermochim Acta 2003;400:61–7.
[50] Barde AA, Klausner JF, Mei R. Solid state reaction kinetics of iron oxide reduction using hydrogen as a reducing agent. Int J Hydrogen Energy 2016;41:10103–19.
[51] Heidari A, Niknahad N, Iljana M, Fabritius T. A review on the kinetics of iron ore reduction by hydrogen. Materials 2021;14:7540.
[52] Zhang, Z., The characteristics and reduction of wustite, in Iron ores and iron oxides - new perspectives, B. Kumar, Ed., IntechOpen, 1–14.
[53] Kakiuti F. REDUSTION YON MAGNETIT ZUR HERSTELLUNG DES SCHWAMMEISENS. (II): reduktion von Groberz. Tetsu-To-Hagane 1942;28:5–10.
[54] Longbottom RJ, Ingham B, Reid MH, Studer AJ, Bumby CW, Monaghan BJ. In situ neutron diffraction study of the reduction of New Zealand ironsands in dilute hydrogen mixtures. Miner Process Extr Metall (IMM Trans Sect C) 2019;128:183–92.
[55] Leubner IH. A balanced nucleation and growth model for controlled precipitations. J Dispersion Sci Technol 2001;22:125–38.
[56] Ham FS. Theory of diffusion-limited precipitation. J Phys Chem Solid 1958;6:335–51.
[57] Zener C. Theory of growth of spherical precipitates from solid solution. J Appl Phys 1949;20:950–3.
[58] John D H St, Matthew SP, Hayes PC. The breakdown of dense iron layers on wustite in CO/CO2 and H2/H2O systems. Metall Trans B 1984;15:701–8.
[59] El Moujahid S, Rist A. The nucleation of iron on dense wustite: a morphological study. Metall Trans B 1988;19:787–802.
[60] Noguchi D, Ohno K, Maeda T, Nishioka K, Shimizu M. Kinetics of reduction step of wustite to iron of hematite and Quaternary calcium ferrite mixtures. ISIJ Int 2013;53:1350–7.
[61] El-Rahaiby SK, Rao YK. The kinetics of reduction of iron oxides at moderate temperatures. Metall Trans B 1979;10:257–69.